THE AMERICAN SOCIETY OF MECHANICAL ENGINEERS
345 E. 47th St., New York, N.Y. 10017

98-GT-344

VARIATIONS IN UPSTREAM VANE LOADING WITH CHANGES IN BACK PRESSURE IN A TRANSONIC COMPRESSOR

Douglas P. Probasco and J. Mitch Wolff
Department of Mechanical & Materials Engineering
Wright State University
Dayton, OH

William W. Copenhaver
Air Force Research Laboratory
Wright-Patterson Air Force Base, OH

Randall M. Chriss
NASA Lewis Research Center
Cleveland, OH

ABSTRACT

Dynamic loading of an inlet guide vane (IGV) in a transonic compressor is characterized by unsteady IGV surface pressures. This pressure data was acquired for two spanwise locations at a 105% speed operating condition, which produces supersonic relative Mach numbers over the majority of the rotor blade span. The back pressure of the compressor was varied to determine the effects from such changes. Strong bow shock interaction was evident in both experimental and computational results. Variations in the back pressure have significant influence on the magnitude and phase of the upstream pressure fluctuations. The largest unsteady surface pressure magnitude, 40 kPa, was obtained for the near stall mass flow condition at 75% span and 95% chord. Radial variation effects caused by the spanwise variation in relative Mach number were measured. Comparisons to a two-dimensional non-linear unsteady blade/vane Navier-Stokes analysis shows good agreement for the 50% span results in terms of IGV unsteady surface pressure. The results of the study indicate that significant non-linear bow shock influences exist on the IGV trailing edge due to the downstream rotor shock system.

NOMENCLATURE

a - speed of sound
b - stream tube thickness
c - chord length
e - internal energy
E - flux vector in m-direction
F - flux vector in θ-direction
H - source term vector
m - meridional coordinate
M - Mach number
p - pressure
Pr - Prandtl number
Q - vector of dependent variables
Re - Reynolds number
r - radial coordinate
S_m - stream tube surface
t - time
u - velocity component in m-direction
v - velocity component in θ-direction
V - contravariant velocity component
x - distance along vane or blade
z - axial coordinate
γ - ratio of specific heats
λ - second coefficient of viscosity(=-2/3μ)
μ - coefficient of viscosity
ω - angular velocity
ρ - density
σ - shear stress
θ - circumferential coordinate

Subscripts

i - inviscid term
n - normalized
s - IGV inlet
v - viscous term
1 - IGV upper surface
2 - IGV lower surface

Presented at the International Gas Turbine & Aeroengine Congress & Exhibition
Stockholm, Sweden — June 2–June 5, 1998
This paper has been accepted for publication in the Transactions of the ASME
Discussion of it will be accepted at ASME Headquarters until September 30, 1998

INTRODUCTION

Gas turbine engines are a vital energy source for both industrial and military applications. Recent research has focused on identifying the flow mechanisms that produce high cycle fatigue (HCF) failures in these engines. There is a need for an improved understanding of the flow physics that drive failures in engine components. This greater understanding will lead to the ability of manufacturers to achieve higher levels of performance and, in general, a more efficient and reliable system. There are continually increasing demands on gas turbine engines for greater durability, reduced noise levels, reduced size and greater thrust. Durability has become a major parameter in component design. Designing compression system components resistant to HCF failure is critical to capitalize on technology improvements. A considerable portion of recent research involves the unsteady interaction between adjacent blade rows which drives HCF in both the compressor and turbine sections.

The two principal types of blade row interaction are usually referred to as potential flow and wake interactions (Verdon, 1992). Potential flow interaction results from the variations in the velocity potential or pressure fields associated with the blades of a neighboring row and their effect upon the blades of a given row moving at a different rotational speed. This type of interaction is of serious concern when the axial spacing between adjacent blade rows is small or the flow Mach number is high. Wake interaction is the effect upon the flow through a downstream blade row of the vortical and entropic wakes shed by one or more upstream rows.

Recently, computational work has been initiated to develop non-linear, time-accurate, inviscid (Euler) and viscous (Navier-Stokes) solution techniques for unsteady flows through isolated and aerodynamically coupled blade rows (see Verdon, 1992 for a review). For coupled systems of rotating and stationary blade rows, the relative motions between adjacent rows give rise to unsteady aerodynamic excitations which can initiate blade vibrations, generate discrete-tone noise, and degrade aerodynamic efficiency.

Some experimental investigations for compression systems have been made into vane/blade interactions. For compressors, initial research was accomplished using low speed rigs (Kim et al., 1992) or annular cascades (Henderson et al., 1992). The low speed and large scale of these experimental rigs simplifies the measurements, but transonic flow phenomena, i.e., shock interaction, can not be modeled. Recently, high speed axial compressor research has been initiated. These facilities are beneficial for testing actual hardware components with research issues including miniature measurement techniques and data reduction methods. In particular, Johnston and Fleeter (1994, 1996, 1997) have used a transonic compressor facility to investigate rotor wake phenomena, IGV/rotor potential fields, and rotor surface pressures using pressure sensitive paints. These research studies have provided an important initial step towards understanding the basic physics of the unsteady aerodynamic flow interactions in a compression system, but additional research is required.

The objective of this research is to investigate and quantify the fundamental vane/blade interaction phenomena relevant to the upstream bow shock forcing function of a downstream rotor in a transonic compression system. This is accomplished by performing a series of experiments in the Compressor Aero Research Lab (CARL), a high speed, highly loaded compressor facility. IGV unsteady surface pressures are experimentally determined for different back pressures for a transonic operating point. In addition, a non-linear, unsteady, fully viscous multi-blade row computational fluid dynamics (CFD) analysis is compared with the experimental data. The CFD code utilized is entitled Vane/Blade Interaction (VBI) which solves the full Navier-Stokes equations through the use of a Runge-Kutta scheme along with the Baldwin-Lomax model for turbulence (Rao et al., 1992). The study presented here will show: 1) bow shock influences from a downstream transonic stage are significant; 2) the bow shock influence grows with increased stage back pressure; 3) the influence can be adequately modeled with an unsteady, non-linear Navier-Stokes analysis; 4) the bow shock influence of a transonic rotor varies with span and must be modeled accordingly, and 5) higher-order harmonic content of unsteady surface pressures is significant and important for transonic vane/blade analyses.

RESEARCH FACILITY

Compressor Aero Research Lab (CARL). The experiments for this study were conducted in the Air Force Research Laboratory's Compressor Aero Research Lab facility at Wright-Patterson Air Force Base. The research compressor is a high speed, highly-loaded 1 1/2 stage compression system. The compressor facility consists of an open or closed loop

(currently open) tunnel system with an upstream venturi flow meter to measure the mass flow rate. The compressor is driven by a 1490 kW electric motor with a variable speed range of 6,000 to 21,500 rpm.

The research compressor, Figure 1, was designed to simulate the second stage of a highly-loaded military core compressor. Wakes from a first stage are simulated by a upstream blade row. The primary intent for this research compressor is to investigate the influence of an upstream stage on the flow swallowing capability of a downstream transonic stage. Details on the compressor design are defined by Law (1989) and are summarized in Table 1.

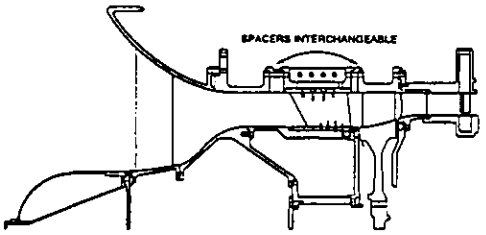

Figure 1. Schematic of SMI Compressor Rig.

PARAMETER	ROTOR	STATOR
Number of Airfoils	33	49
Aspect Ratio - Average	0.961	0.892
Inlet Hub/Tip Ratio	0.750	0.816
Flow/Annulus Area, kg/sec	18.14	--
Flow/Unit Area, kg/sed/m²	0.738	--
Flow rate, kg/sec	15.63	--
Tip Speed, Corrected m/sec	341.4	--
M_{REL} LE Hub	0.963	0.820
M_{REL} LE Tip	1.191	0.690
PR Rotor	1.880	--
η_{isq} Rotor, %	93.5	--
PR Stage	--	1.840
η_{isq} Stage, %	--	90.2
D Factor Hub	0.545	0.502
D Factor Tip	0.530	0.491
LE Tip Dia., m	0.4826	0.4826
LE Hub Dia., m	0.3620	0.3928
TE Tip Dia., m	0.4826	0.4826
TE Hub Dia., m	0.3872	0.4038

Table 1. Compressor Design Parameters

To study the effect of different upstream stages, an IGV assembly is placed upstream of the rotor section. The IGV's were designed to create a wake consistent with a modern technology, highly-loaded, low aspect ratio stage. Therefore, they have a wide trailing edge as shown in Figure 2. The IGV's do not turn the flow as would a normal IGV assembly. They have a constant solidity (spacing to chord ratio) along the span and have no steady aerodynamic loading in order to achieve a uniform two-dimensional wake. There are 24 IGV's in the upstream passage. The axial spacing between the IGV blades trailing edge and the rotor leading edge is 26% of the rotor chord.

IGV Surface Pressure Instrumentation. The IGV's are instrumented with miniature Kulite pressure transducers. Figure 3 shows the locations of these pressure transducers. Two different blades are instrumented with 10 pressure transducers each. To investigate spanwise effects, two different spanwise locations are instrumented, 50% and 75% as shown measured from the hub. A picture of the actual mounted transducers for one blade is shown in Figure 4. The blade surface is machined to allow the pressure transducers to be mounted flush. To protect the pressure sensor, a thin layer of RTV was placed over the diaphragm. Grooves for the lead wires were also machined to ensure no disturbance to the flow. The lead wires are bundled and fed out of the casing.

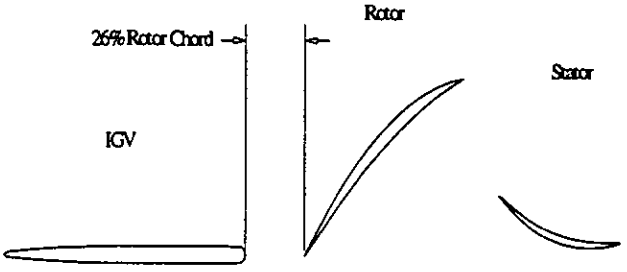

Figure 2. Flow path through SMI Compressor Rig

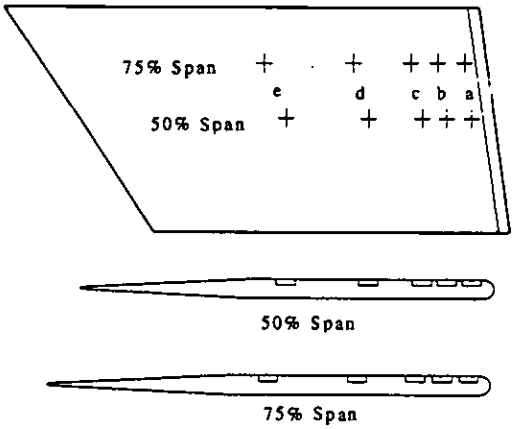

Figure 3. Transducer Locations on IGV. (a)95% (b)89% (c)83% (d)70% (e)50% IGV chord

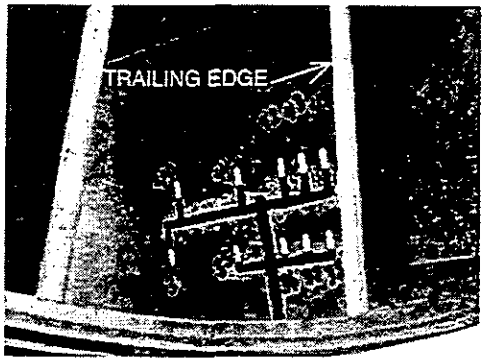

Figure 4. Actual transducer application on IGV

Two adjacent IGV's are instrumented giving data for one flow passage. Flow periodicity is assumed with one blade's data phase shifted to the other blade for analysis.

LQ-125 miniature pressure transducers from Kulite are used for the surface pressure measurements. These transducers were designed to measure absolute pressure up to 172.4 kPa. The pressure transducers are manufactured directly on the blades with a pressure sensing element 0.1524 cm in diameter. It has an internally compensated temperature range of -1.1 to 54.44°C. The natural frequency of the pressure transducer is specified as 300 kHz, giving a usable frequency range of 100 kHz.

Calibration of the transducers for sensitivity and offset was achieved through bench tests. Before installation of the instrumented IGV, the transducers were subjected to variable pressures at a nominal temperature of 21.1°C and an elevated temperature of 43.3°C. The results of this study indicated, for this range of temperature variation, transducer sensitivity was 0.02% per degree C. However, the offset was influenced by temperature variation and the magnitude of the shift varied from a high of 0.2516 kPa/°C to a low of 0.0148 kPa/°C.

Based on this bench calibration, no special procedures were established to control sensitivity with inlet air temperature shifts. However, to control transducer offset variation, the transducers' amplifiers were re-balanced at atmospheric conditions for any inlet temperature shift of 1.4°C or greater.

From these bench procedures, offset and precision errors were established as ±0.414 kPa and ±0.276 kPa, respectively. In addition, during the experiment, a zero response data set was recorded. The data was then processed in the same manner as the actual test data. This signal is representative of the static pressure uncertainty due to system noise influences. Based on all of the above calibration and operating procedures, the measured random uncertainty was ±0.689 kPa. This value includes all errors due to random noise and temperature changes.

COMPUTATIONAL ANALYSIS

A non-linear unsteady Euler/Navier-Stokes vane blade interaction model, VBI 2D, was developed by Rao et al. (1990), under sponsorship of the Air Force, for turbine configurations. This model analyzes the relative motion of adjacent blade rows by allowing one row to move with respect to the other. The VBI code is utilized for the IGV/rotor interaction in the compressor by modeling both the IGV and rotor. A brief overview of the VBI code will now be given.

Grid Generation. Two separate grids are generated which are an H and O grid for each blade row. The two grids are then embedded to form a composite grid by a chimera method called PEGSUS (Benek et al., 1987). PEGSUS creates the appropriate hole boundaries and interpolation stencils involved in the communication of embedded grids. The embedding process eliminates problems with cell skewness near the leading and trailing edges of the airfoils. The transition from the inflow and outflow boundaries to the airfoil leading and trailing edges causes this problem. The PEGSUS results are read directly into the VBI code.

Numerical Method. The VBI code solves the Euler/Navier Stokes equations using an explicit Runge-Kutta scheme in quasi-three-dimensional space. Figure 5 represents

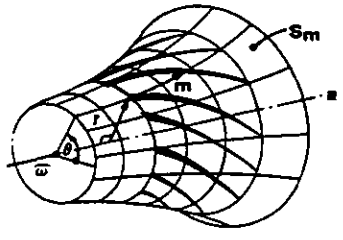

Figure 5. Coordinate system used in VBI formulation

the coordinate system used in the formulation (Rao et al., 1992). The Baldwin-Lomax (Baldwin et al., 1978) model for turbulence and transition is utilized within the code. The governing equations for flow on a

blade-to-blade surface of revolution will now be given (Rao et al., 1992):

$$\frac{\partial Q}{\partial t}+\frac{\partial E}{\partial m}+\frac{\partial F}{\partial \theta}=H \qquad (1)$$

where:

$$H=H_i-H_v+\frac{\partial E_v}{\partial m}+\frac{\partial F_v}{\partial \theta}$$

$$Q=rb\begin{bmatrix}\rho\\ \rho u\\ \rho v\\ \rho e\end{bmatrix} \qquad E=rb\begin{bmatrix}\rho u\\ \rho u^2+p\\ \rho uv\\ u(\rho e+p)\end{bmatrix}$$

$$F=b\begin{bmatrix}\rho v\\ \rho uv\\ \rho v^2+p\\ v(\rho e+p)\end{bmatrix} \qquad E_v=\frac{rb}{\mathrm{Re}}\begin{bmatrix}0\\ \sigma_{11}\\ \sigma_{12}\\ E_4\end{bmatrix}$$

$$F_v=\frac{b}{\mathrm{Re}}\begin{bmatrix}0\\ \sigma_{12}\\ \sigma_{22}\\ F_4\end{bmatrix} \qquad H_i=rb\begin{bmatrix}0\\ \left(\rho v^2+p\right)\frac{1}{r}\frac{dr}{dm}+p\frac{1}{b}\frac{db}{dm}\\ -\rho uv\frac{1}{r}\frac{dr}{dm}\\ 0\end{bmatrix}$$

$$H_v=\frac{rb}{\mathrm{Re}}\begin{bmatrix}0\\ \sigma_{22}\frac{1}{r}\frac{dr}{dm}+\sigma_{33}\frac{1}{b}\frac{db}{dm}\\ -\sigma_{12}\frac{1}{r}\frac{dr}{dm}\\ 0\end{bmatrix}$$

The following equations represent the energy components

$$e=\frac{p}{\rho(\gamma-1)}+\frac{1}{2}\left(u^2+v^2\right) \qquad (2)$$

$$E_4=u\sigma_{11}+v\sigma_{12}+\frac{1}{\gamma-1}\frac{\mu}{\mathrm{Pr}}\frac{\partial a^2}{\partial m} \qquad (3)$$

$$F_4=u\sigma_{12}+v\sigma_{22}+\frac{1}{\gamma-1}\frac{\mu}{\mathrm{Pr}}\frac{1}{r}\frac{\partial a^2}{\partial \theta} \qquad (4)$$

where E_4 and F_4 are the viscous terms from the energy equation. It is now necessary to represent the shear stress equations:

$$\sigma_{11}=2\mu\frac{\partial u}{\partial m}+\lambda\nabla\cdot V \qquad (5)$$

$$\sigma_{12}=\mu\left(\frac{\partial v}{\partial m}-\frac{v}{r}\frac{dr}{dm}+\frac{1}{r}\frac{\partial u}{\partial \theta}\right) \qquad (6)$$

$$\sigma_{22}=2\mu\left(\frac{1}{r}\frac{\partial v}{\partial \theta}+\frac{u}{r}\frac{dr}{dm}\right)+\lambda\nabla\cdot V \qquad (7)$$

$$\sigma_{33}=2\mu\frac{u}{b}\frac{db}{dm}+\lambda\nabla\cdot V \qquad (8)$$

For this analysis, it is assumed that Stokes' hypothesis is true. For turbulent results, the viscosity is represented in an appropriate form. The laminar and turbulent viscosities are accounted for with the turbulent viscosity found from the Baldwin-Lomax eddy-viscosity model.

Boundary Conditions. Non-reflective inflow and outflow boundary conditions are utilized for the H-grids with a reference plane method of characteristics scheme. For the O-grids, the reference planes are inherently non-parallel due to the fact that they are conforming to the airfoil shapes. It is then necessary for the VBI code to set the reference planes parallel to each other and perpendicular to the inflow boundary. This allows for the reference plane method of characteristics scheme to successfully be utilized at these boundary points. As the blade moves relative to the vane with the progression of a time step, the information from the previous time step is used to define the necessary vane outflow or blade inflow boundaries.

A phase-lagged technique is utilized for the blade to blade periodic boundary conditions. The computation is performed on one vane or blade from each row at a time. The solution fields for adjacent vanes or blades are stored for the use in the phase-lagging procedure (Rao et. al, 1992).

An overlapping of the H-grids at the vane outlet and blade inlet allows for information to passed from one row to another. At least three cells must overlap for accurate information exchange. A bi-linear interpolation method is used to transfer the data from the IGV H-grid to the rotor H-grid to find the necessary boundary conditions.

RESULTS

A series of experiments were performed to investigate the IGV unsteady surface pressure response due to the upstream traveling pressure field generated by the downstream rotor. The stage back pressure was varied by exit area changes and the IGV response measured at two spanwise positions. A computational study was then completed utilizing the VBI code with comparisons made to the experimental data.

Experimental. The experimental data was recorded on a 28 channel analog tape recorder with a flat response up to 80 kHz. The data was digitized off-line at an effective sample rate of 500 kHz by reducing the tape playback speed by one quarter and sampling at 125 kHz. Anti-aliasing was achieved using a Precision Filters TD6B Linear Phase Time

Delay Filter. An effective cutoff frequency of 132 kHz was used for the data reduction. This gives a 1% attenuation of the signal at 77 kHz. The blade pass frequency is 7.8 kHz. Therefore, the first 11 blade pass harmonics are resolved without aliasing or attenuation. Data was digitized for a time record of 68 milliseconds as was dictated by storage limitations, which gives approximately 11 rotor revolutions. Ensemble averaging was performed on the data in order to average out any inconsistencies that may exist from one rotor blade to the next. The ensemble averaging was accomplished based on the rotor blade pass frequency; since the rotor has 33 blades, about 363 records were ensemble averaged. To assist in discussion of the results, the data is presented as two blade passages from the same averaged single passage record.

For an analysis of the effects of back pressure on the surface pressure variations on the IGV's, the 105% corrected rotor speed was used with a 26% rotor chord spacing. This spacing is very representative of typical compressor designs. At 105% corrected rotor speed, the relative Mach number at 75% span is 1.22 and at 50% span is 1.14. A nondimensionalized difference of the pressure values across the blade was determined from the measured absolute pressure data as defined by Equation 9.

$$p_n = \frac{p_1 - p_2}{p_s} \tag{9}$$

Back Pressure Influence: Five different back pressures were used defining a complete speed line, as detailed in Figure 6. They were open throttle (point a), peak efficiency (point c), near stall (point e) and two other points in between (points b and d). The experimental results from all five back pressures are shown on the same plot for comparison at each chordwise location. Averaged time-resolved results from both spanwise locations are presented in Figures 7 and 8 with only four chordwise measurements shown due to a lost transducer at 75% span and 50% chord.

Figure 7d represents the data at the 50% span, 95% chord location. At this chord location, the near stall back pressure is where the unsteady pressure loading is the highest. The overall magnitude of this unsteady loading is a normalized pressure of approximately 0.32. This translates into a pressure variation of 29.65 kPa, which is quite substantial within a compressor from a structural point of view. The results presented in Figure 7d are consistent with the governing flow physics concerning transonic compressor operation and variations in back pressure (Pierzga et al., 1985). As the back pressure is increased, the mass flow rate is decreased. Once on the horizontal portion of the charcteristic (Points b-e), the downstream back pressure increase will push the compressor bow shock further upstream from the blade leading edge resulting in a stronger bow shock and also a phase lead, relative to the rotor blade, in sensing the shock influence on the IGV. This concept is demonstrated in Figure 9. Therefore, the bow shock will move forward and be sensed earlier on the IGV as the back pressure is increased with a maximum value found at the near stall location. As will be demonstrated in all the results presented, this trend is consistently found experimentally.

Even though the bow shock wave is weaker at the open throttle position, a substantial unsteady pressure fluctuation is shown. Its normalized value is 0.12 (11.03 kPa). The change in phase, with respect to the rotor leading edge, of the unsteady pressure loadings with variations in back pressure are clearly shown in Figure 7d. As the flow rate is increased from the near stall condition to the open throttle condition, Figure 7d shows a continually increasing phase lag in the unsteady surface pressure values. This result is consistent with the previous description of the bow shock movement with an increase in back pressure, as desribed in Figure 9. The further the shock's position is upstream of the rotor leading edge, the earlier it will reach the IGV's. This effect is also shown by considering the phase information from a first harmonic Fast Fourier Transform analysis of the data. Figure 10 shows the first harmonic phase results for the five different back pressures. As the flow rate is decreased the phase plots are continually shifted forward.

Figure 7c shows the results at 89% chord. Again, the near stall back pressure has the largest overall pressure fluctuation, 0.16 or 14.48 kPa. In comparison with Figure 7d, the unsteady pressure magnitudes have decreased due to viscous dissipation as the pressure wave moves upstream. The bow shock's strength weakens the further upstream it travels, but the shock is definitely present at the 89% chord location for the near stall back pressure. Similar trends are found at the 83% and 70% chord locations, Figures 7b and 7a, as the 95% and 89% chord results just discussed.

In review of the 50% spanwise results, several statements can be made. Back pressure plays a significant role in the magnitude of the unsteady surface pressure fluctuations measured on the IGV by the downstream transonic rotor. The higher the back pressure, the further the bow shock's location moves upstream. Therefore, stronger unsteady surface pressures are experienced by the IGV's. As the back

pressure was increased, the unsteady pressure histories show a continually increasing phase shift in the results. This trend holds for all chordwise locations as shown in Figure 10. Finally, the further upstream on the IGV's, the weaker the pressure fluctuations measured on the IGV surface.

Spanwise Variations: To investigate three-dimensional effects, instrumentation was applied at the 75% spanwise location at the same chordwise locations as the 50%. Figure 8 shows the results from the 75% span transducers for 105% speed. Due to the increased radial distance at 75% span, the rotor blade speed is higher resulting in a higher relative Mach number (1.22 vs. 1.14). It is expected this higher Mach number will result in a stronger bow shock and increased unsteady IGV surface pressure measurements over those at 50% span.

The near stall back pressure results in Figure 8d show the greatest unsteady pressure fluctuation of 0.43 normalized or 40 kPa. This is a significant increase over the 29.65 kPa at the 50% span, 95% chord location. The pressure data from the peak efficiency back pressure has a maximum magnitude of approximately 0.19 or 17.24 kPa. All trends seen at the 50% spanwise location are duplicated at 75% span, however the magnitude changes are more pronounced. Figure 11 shows the first harmonic unsteady phase distribution with IGV chord. As the back pressure is decreased, the phase distribution shifts ahead. At 75% span, the effect of the bow shock at the 95% chord location is quite evident at all flow rates. When compared to the 50% span results, the 75% span results show the increased bow shock strength of the transonic rotor downstream of the IGV's. The trends for the remainder of the chord locations upstream (Figures 8a and 8b) are the same as the 95% chord data, which was true at the 50% span as well.

As was shown, all of the trends at the 50% spanwise location were true at the 75% span. Therefore, the unsteady pressure magnitude decreases with decreasing back pressure, the phase relationship moves forward with decreasing back pressure, and the pressure magnitude increases in moving closer to the trailing edge. In addition, when compared to the 50% span results, significant spanwise variations are evident. These effects are caused by the change in rotor relative Mach number with radial location. The first harmonic unsteady pressure magnitudes, Figure 12, show a spanwise location effect as well as the fact that the pressure magnitude increases in moving towards the IGV trailing edge. The first harmonic magnitude of the 75% span is significantly larger than that of the 50% span and the magnitudes at the 95% chord location are dominant with the values then dropping off with movement upstream along the IGV surface.

Harmonic Content: Another important discovery is significant higher-order harmonic content within the unsteady pressure signals. Figure 13 demonstrates this fact for both the 50% and 75% span data through a Fast Fourier Transform analysis. The blade pass frequency is dominant for the 75% span data but the second harmonic is significant in magnitude. The 50% span data shows that the second harmonic is actually dominant. The power of the higher-order harmonics for both spanwise positions decrease significantly past the second. In order to properly model or analyze vane/blade interactions, it is necessary to take the higher-order harmonic content into account. The magnitude at the blade pass frequency is generally dominant but the fluctuations that occur above this frequency can be important as well, thereby creating a necessity to perform a non-linear analysis.

Computational. A comparison of computational results and experimental data will be shown. The operating point used for this comparison is the 105% corrected speed, near stall back pressure. This operating point is shown in Figure 6. A grid independence check was done for the computational work and the number of grid points for both the H and O-grids for each row will now be given. For the IGV row, the O-grid contains 281x27 points and the H-grid, 257x93. The rotor O-grid needed 391x27 points and the H-grid, 289x93, for grid independence. Four thousand and four hundred time steps were used per rotor blade pass with 148,000 time steps needed for convergence. Figure 14 represents a pressure-time history for a node in between the IGV trailing edge and the rotor leading edge for the near stall operating point. A total of 37 rotor blade passes were analyzed to reach a nearly periodic solution as shown in Figure 14. The rotor passage has a 30% stream tube contraction so this value was input into the VBI code to account for the spanwise component of the quasi-three-dimensional analysis. An algebraic turbulence model is utilized to model viscous effects in the computational results presented. Finally, in modeling the current configuration, 24 IGV's and 33 rotor blades, it was possible to reduce the numbers down to 8 IGV's and 11 blades due to periodicity. A phase-lagged boundary condition is then utilized making it necessary to perform the computations on only one vane or blade of each row at a time through the use of storage of data from previous blade positions with

respect to the IGV. The analysis using the reduced 8 IGV's and 11 rotor blades can be seen in Figure 15..

Figure 15 represents the computational Mach contour lines for 11 rotor blades and 8 inlet guide vanes for this near stall back pressure at 50% span. For this operating point, a bow shock at the leading edge of the rotor is known to exist. The high back pressure needed to operate at this low flow rate forces the bow shock upstream of the rotor leading edge. In the computational analysis, the bow shock is clearly evident and is upstream of the rotor leading edge. The Mach numbers before and after the shock match experimental values reasonably, an indication of the solution accuracy. The upstream shock interaction causes a significant unsteady pressure force on the IGV's.

The rotor trailing edge separation noted in Figure 15 is thought to be due to the 2-D analysis (lack of 3-D relief) as well as a low Reynolds number limitation in the turbulence model so that the physics may not be completely captured in part of the blade boundary layer, leading to separation. However, this is thought to have little effect on the upstream solution and the bow shock considered in the present work.

A comparison of the frequency response between the experimental data and computational results is shown in Figure 16. The 95% chord location data was used for this analysis. Figure 16 demonstrates excellent agreement in both frequency and magnitude. The higher-order harmonics are captured by the computational analysis.

A comparison of the local blade loading on the IGV's is shown in Figure 17. The computational results shown are for the last two blade passes of the 37 total. As can be seen in the figure, the interaction weakens from the trailing edge to the leading edge. At the 95% chord location, both the experiment and computations show the steep pressure rise due to the bow shock, with the results showing reasonable agreement in magnitude and phase. For the 89% chord location, Figure17d, the shock structure is still the dominating physical phenomenon. The computational analysis slightly overpredicts the unsteady magnitude response with the phase in excellent agreement. At 83% chord, the results show that the shock has dissipated somewhat and that this dissipation is underpredicted in the simulation. However, the results still show good phase agreement. The comparisons for 70% and 50% chord show relatively poor agreement. Although in reasonable agreement in magnitude, the simulation shows little weakening in shock strength together with poor phase agreement.

The computational model predicted the magnitude and phase of the unsteady pressure on the IGV surface very well for the operating point used for this study. The computation demonstrates the complex character of the unsteady loading as was seen in the experiment, thereby capturing the higher harmonic content that is present in this interaction. The code however did tend to underpredict the shock dissipation in moving upstream along the IGV. From our study, the code predicted the unsteady loading accurately enough to potentially be useful for HCF analyses on blade rows upstream of a rotor row.

SUMMARY AND CONCLUSIONS

This study quantifies the potential influence of a compressor rotor on an upstream IGV. The rotor's influence on the unsteady IGV surface pressure distribution was established experimentally and simulated computationally.

This study reports results from a transonic core compressor stage typical of current military in-service flight hardware. The IGV/rotor spacing is also typical of current in-service hardware.

The rotor's influence on the unsteady IGV surface pressure distribution was quantified at two spanwise locations (50% and 75%) experimentally. In addition, a 2-D unsteady Navier-Stokes solver was used to predict the unsteady surface pressure distribution at 50% span.

The unsteady surface pressure measurements show a higher than expected influence on the IGV, which is due solely to the influence of the downstream rotor. The peak instantaneous local loading was found to be 40 kPa. The bow shock influence increased as the compressor was throttled, i.e., as the stage exit back pressure was increased.

The experiment showed a steep pressure gradient induced by the rotor bow shock wave. Spectral analysis of the time-resolved pressure history contained significant harmonic content, which suggests that the bow shock is the dominant influence on the IGV pressure field. In addition, the spectral analysis showed that the second harmonic is of the same order of magnitude as the first, indicating that first-order models of this type of bow shock interaction may not adequately predict this flow phenomena.

In addition, the experiment showed a significant difference in the upstream influence (IGV unsteady surface pressures) with span, indicating that spanwise effects are deemed to be important in transonic compressor analysis.

The numerical simulation showed that a 2-D computation may be quite useful in predicting upstream potential forcing functions due to downstream blade rows. The code was better able to

predict the bow shock interaction near the IGV trailing edge, while the results further upstream show that the code overpredicts the strength of the bow shock wave.

The computation also demonstrated the capability to predict the complex nature of the forcing function by showing similar harmonic content as was shown in the experimental results. These results show that 2-D unsteady computations show promise in forecasting unsteady blade surface pressure distributions which may be useful in the study of forced blade response.

ACKNOWLEDGMENTS

The authors would like to thank Dr. Herb Law, Mr. Steve Gorrell, Mr. Ron Berger, Mr. Bob Wittig, Mr. Bill Uhlman and Mr. Terry Norris at CARL for their excellent support in obtaining the experimental data. The data quality is a true testament to their dedication towards excellence. The authors would also like to thank Dr. Rolf Sondergaard and Mr. Charles Stevens from AFRL/PRTT for help with the computational results. In addition, the authors acknowledge the Air Force Office of Scientific Research for their financial support in this effort through the summer research program and an extension grant. Finally, this work was supported in part by a grant of HPC time from the DoD HPC Center, MSRC at Wright Patterson Air Force Base through the use of the HPC03 and CFS01 machines.

REFERENCES

Baldwin, B., and Lomax, H., 1978, "Thin Layer Approximation and Algebraic Model for Separated Turbulent Flows," *AIAA Paper No. 78-257.*

Benek, J.A., Donegan, T.L., Suhs, N.E., 1987, "Extended Chimera Grid Embedding Scheme with Application to Viscous Flows," *AIAA Paper No. 87-1126-CP.*

Henderson, G.H., Fleeter, S., 1992, "Airfoil Wake and Linear Theory Gust Response Including Sub and Super-resonant Flow Conditions," *AIAA Paper No. 92-3074.*

Johnston, R.T., Feiereisen, J.M., Fleeter, S., 1994, "Rotor Wake and Potential Forcing Functions, Including Blade Row Interactions," *AIAA Paper No. 94-2975.*

Johnston, R.T., Fleeter, S., 1996, "Time-Resolved Variations of an IGV Flow Field in the Presence of a Rotor Potential Field," *AIAA Paper No. 96-2670.*

Johnston, R.T., Fleeter, S., 1997, "Rotor Blade Pressure Measurement in a High Speed Axial Compressor Using Pressure and Temperature Sensitive Paints," *AIAA Paper No. 97-0162*

Kim, K.H., Fleeter, S., 1992, "Compressor Blade Row Unsteady Aerodynamic Response to Attached and Separated Flow Forcing Functions," *AIAA Paper No. 92-0147.*

Law, C.H., 1989, "Two Axial Compressor Designs for a Stage Matching Investigation," AFWAL-TR-89-2005.

Pierzga, M.J., Wood, J.R., 1985, "Investigation of the Three-Dimensional Flow Field Within a Transonic Fan Rotor: Experiment and Analysis," *Journal of Engineering for Gas Turbines and Power,* Vol. 107, No. 2, pp. 436-449.

Rao, K.V., Delaney, R.A., Topp, D.A., 1992, "Turbine Vane-Blade Interaction," *Interim Report WL-TR-92-2002.*

Rao, K., and Delaney, R., 1990, "Investigation of Unsteady Flow Through Transonic Turbine Stage; Part 1: Analysis," *AIAA paper no. 90-2408.*

Verdon, J.M., 1992, "Unsteady Aerodynamic Methods for Turbomachinery Aeroelastic and Aeroacoustic Applications," *AIAA Paper No. 92-0011.*

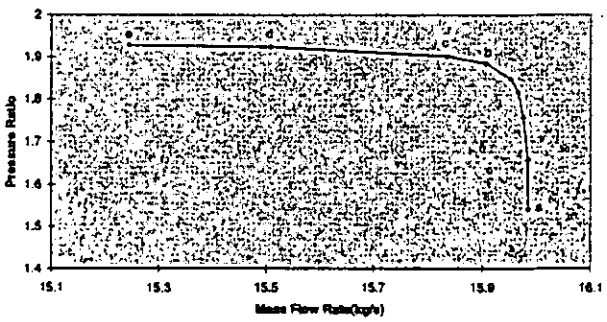

Figure 6. Compressor Performance Map for a)Open Throttle b)Above Design c)Peak Efficiency d)Below Design e)Near Stall

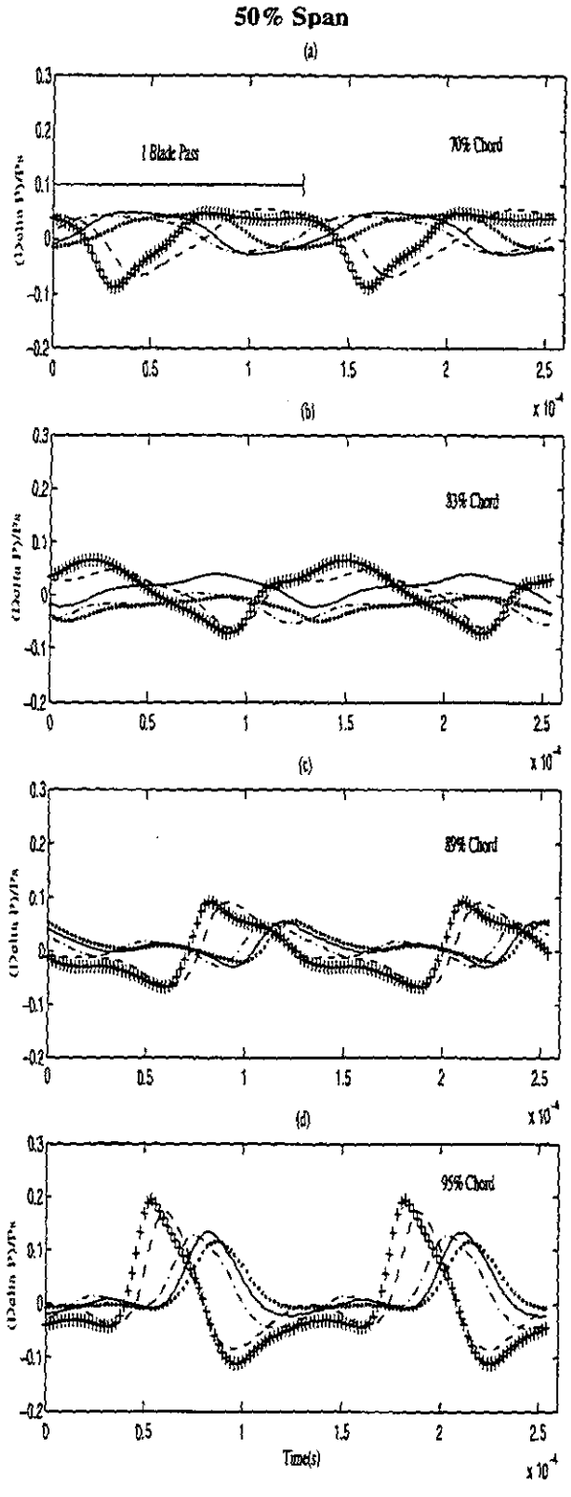

Figure 7. Differenced Nondimensionalized Pressure Time Traces for Various Back Pressures at 50% Span and Different Chordwise Positions on IGV: (a) 70% (b) 83% (c) 89% (d) 95%.

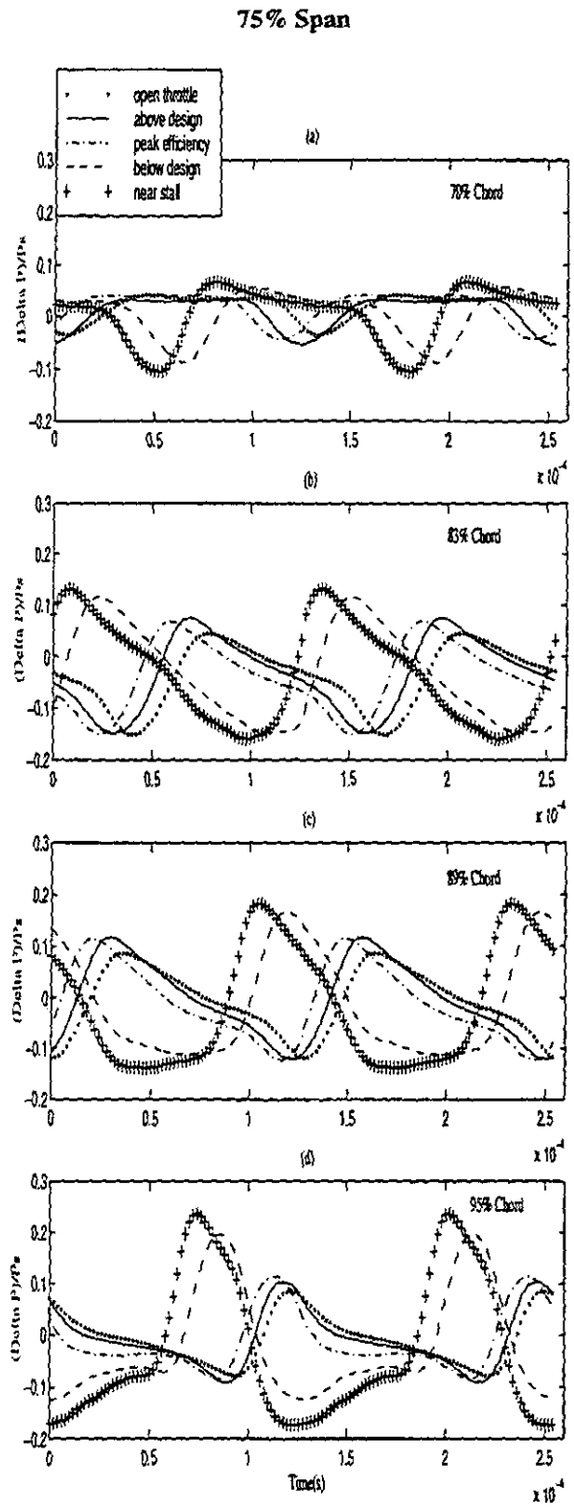

Figure 8. Differenced Nondimensionalized Pressure Time Traces for Various Back Pressures at 75% Span and Different Chordwise Positions on IGV: (a) 70% (b) 83% (c) 89% (d) 95%.

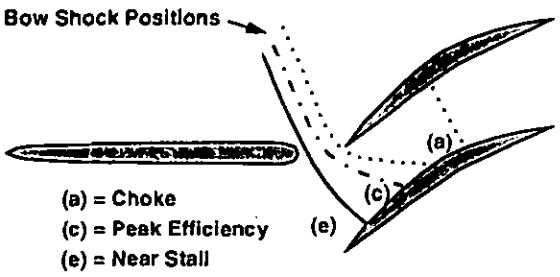

Figure 9. Sketch of Various Shock Positions

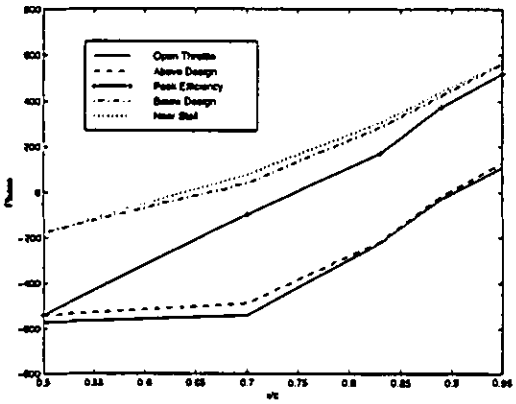

Figure 10. First Harmonic Unsteady Delta Pressure Phase Results - 50% Span

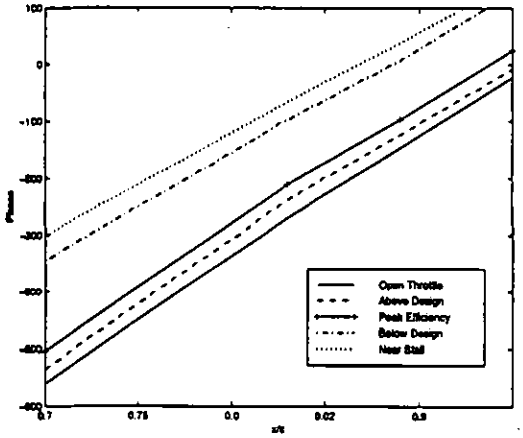

Figure 11. First Harmonic Unsteady Delta Pressure Phase Results - 75% Span

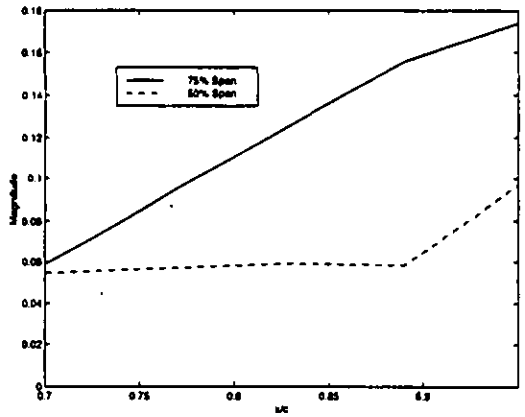

Figure 12. Comparison of First Harmonic Magnitude for 50% Span and 75% Span - Near Stall

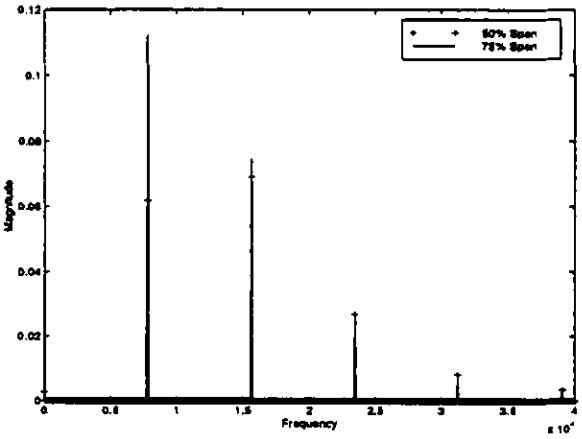

Figure 13. FFT of Near Stall - 95% Chord Experimental Data

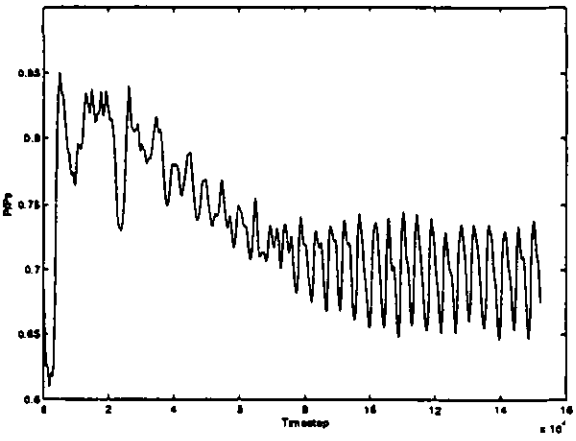

Figure 14. Pressure Time History for Convergence Check

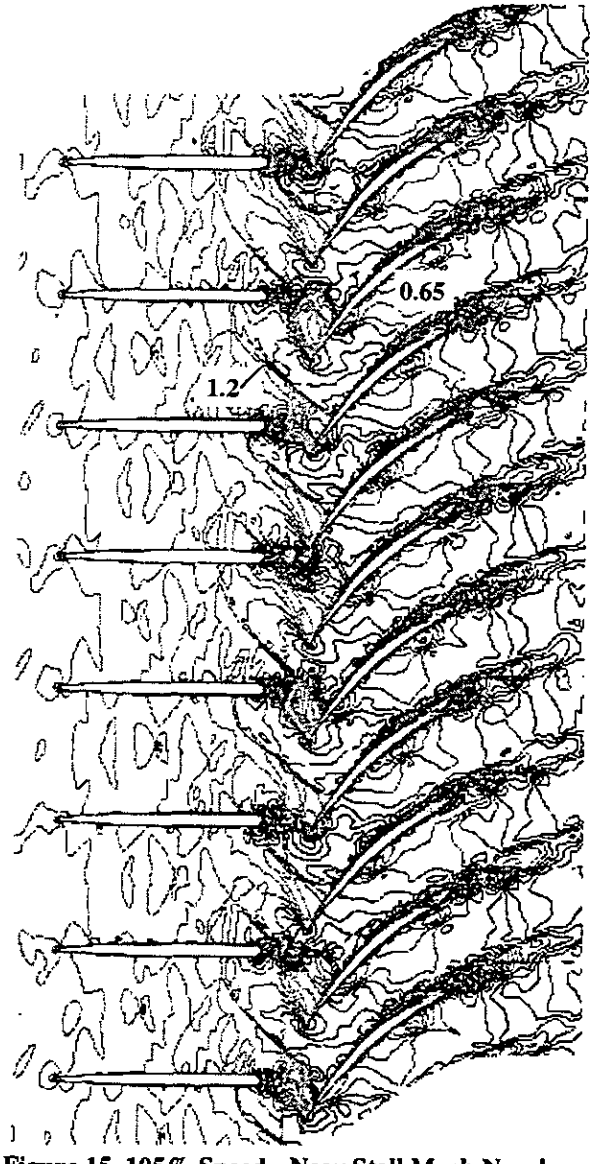

Figure 15. 105% Speed - Near Stall Mach Number Contours - 50% Span

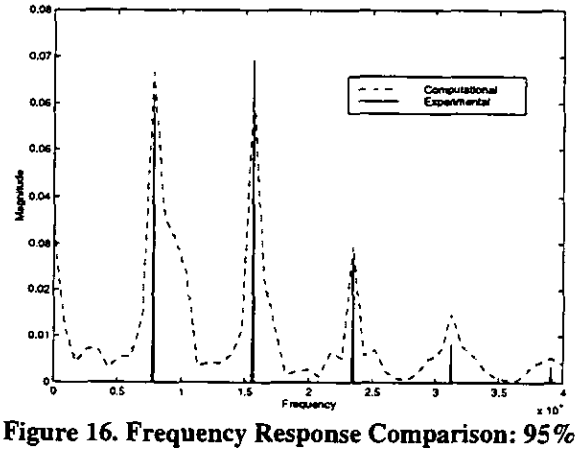

Figure 16. Frequency Response Comparison: 95% Chord 50% Span

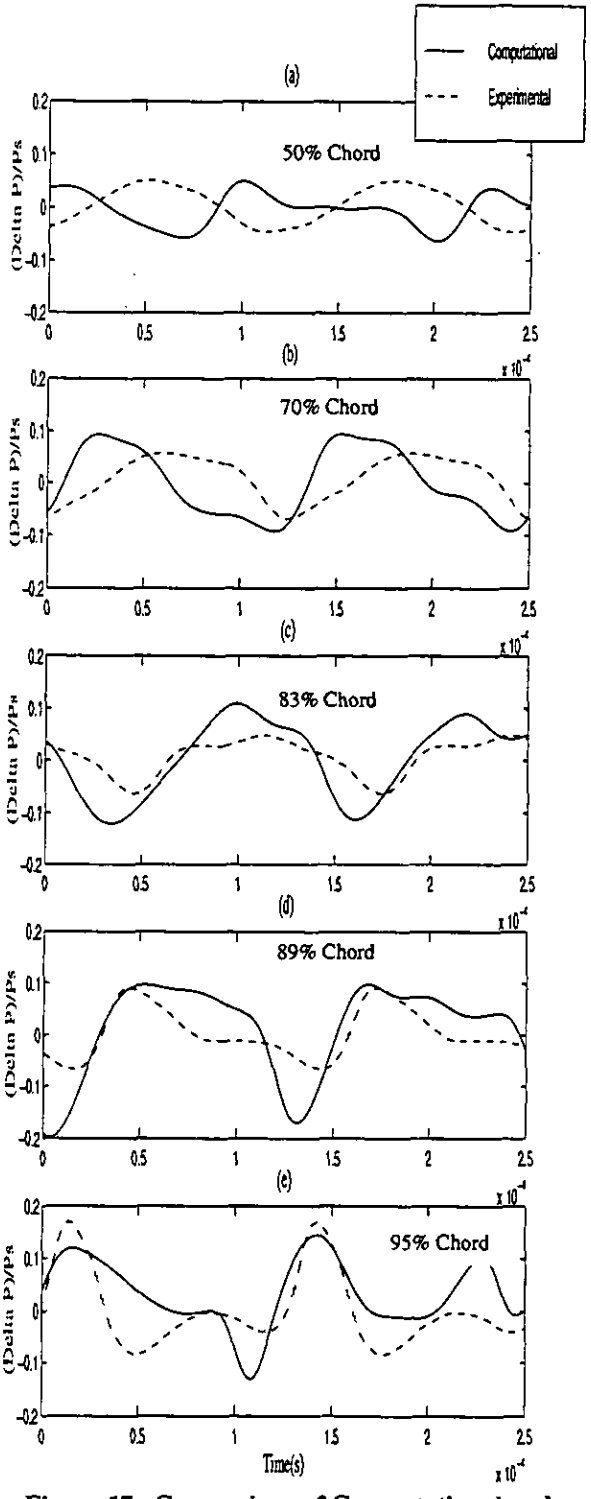

Figure 17. Comparison of Computational and Experimental Pressure for Near Stall (a) 50% (b) 70% (c) 83% (d) 89% (e) 95% Chord Location on IGV.